Materials & Design 266 (2026) 116222

Contents lists available at ScienceDirect

Materials & Design

journal homepage: www.elsevier.com/locate/matdes

Anomalous grain growth as a pathway toward fully single-crystallization in IN738LC Ni-based superalloy fabricated by laser powder bed fusion☆

Masayuki Okugawa [a,b,*], Kazufumi Nose [a], Sei Hirooka [a], Sukeharu Nomoto [a,c], Yuheng Liu [a], Makoto Watanabe [c], Yuichiro Koizumi [a,b,*], Takayoshi Nakano [a,b]

[a] Graduate School of Engineering, The University of Osaka, 2-1 Yamadaoka, Suita, Osaka 565-0871, Japan
[b] 3DPTec Integrated Center, The University of Osaka, Suita 565-0871, Japan
[c] Research Center for Structural Materials, National Institute for Materials Science, Ibaraki 305-0047, Japan

ARTICLE INFO

Keywords:
Additive manufacturing
Laser powder bed fusion
Ni-based superalloy
Single-crystal fabrication
μ-Helix scan

ABSTRACT

The application of additive manufacturing (AM) to Ni-based superalloys has attracted considerable attention because it enables the production of high-temperature parts that are lighter, integrally formed, and less expensive. However, single-crystal fabrication of precipitation-hardened Ni-based superalloys using AM remains challenging. This study demonstrates that a single crystal (SX) of the IN738LC Ni-based superalloy can be fabricated via laser powder bed fusion (PBF-LB) and the quality of the built SX part can be improved via optimal thermal annealing. The as-fabricated part exhibits inhomogeneities in crystal orientation: the central area is a single crystal, whereas the edges are polycrystalline. The crystal orientation of the single-crystal region is largely affected by gas flow during the build, which could be detected by the in-process melt pool monitoring system. Additionally, significant solute-element segregation is observed in the microstructure of the single-crystal region, consistent with the distribution predicted by the multi-phase-field simulation. Notably, we found that anomalous grain growth, induced by optimal annealing at 1200 °C, selectively expands the SX region while eliminating solute-element segregation, thereby improving the overall quality of the single-crystal part. These findings provide insight into the development of single-crystal fabrication via the PBF-LB process for aerospace and energy applications.

1. Introduction

Single-crystal (SX) growth of Ni-based superalloys has been investigated for applications in high-temperature environments [1], such as in jet-engine turbines and power generation, because grain boundaries often serve as crack initiation sites in these environments. Further increases in the operating temperatures of SXs are required to meet the demands for improving the efficiency, output, and durability of their applications.

Additive manufacturing (AM) technologies have attracted attention for the fabrication of Ni-based superalloys [2,3]. AM can easily build three-dimensional (3D) parts with complex geometries, and the operating temperature of the parts can be increased by optimizing cooling channels. Among the wide range of AM techniques available, powder bed fusion (PBF) is a preferred technique for metal AM [4–8]. In the PBF process, metal products are built layer-by-layer by scanning laser or electron beams, which fuse the metal powder particles into bulk solids, and epitaxial growth occurs during solidification in the direction of the temperature gradient perpendicular to the solid–liquid interface [9,10]. Thus, achieving a specific crystallographic texture within the product has recently become possible by optimizing the scanning conditions [11–14]. Although there are small local angular differences in the solid–liquid interface direction of the melt pool, the growth orientations align as the layering progresses under appropriate process conditions.

Numerous studies have aimed to use PBF techniques to obtain SX parts composed of pure Ni [15] and Ni-based superalloys, such as IN718 [16–18], IN-738 [19], Haynes 282 [19,20], SRR99 [21], CMSX-4 [22], and Hastelloy-X (HX) [23]. Recently, an SX IN718 alloy with a uniform crystal orientation in the electron backscatter diffraction (EBSD)–inverse pole figure (IPF) map was obtained using electron beam (EB)-PBF with the μ-helix scanning strategy as reported in Ref. [18]. This strategy mimics the conventional selector method in the casting process for SX

☆ This article is part of a special issue entitled: 'Additive Manufacturing' published in Materials & Design.

* Corresponding authors at: Graduate School of Engineering, The University of Osaka, 2-1 Yamadaoka, Suita, Osaka 565-0871, Japan.
E-mail addresses: okugawa@mat.eng.osaka-u.ac.jp (M. Okugawa), ykoizumi@mat.eng.osaka-u.ac.jp (Y. Koizumi).

https://doi.org/10.1016/j.matdes.2026.116222
Received 17 February 2026; Received in revised form 1 May 2026; Accepted 12 May 2026
Available online 14 May 2026

growth. Fig. 1 shows schematic illustrations of the μ-helix method: the μ-helix scan simulates the conventional SX growth selector method, in which a single crystal is grown by unidirectional solidification as it passes through a mold with a spiral channel. In the μ-helix method, narrowing the scan line spacing allows adjacent beam scans to overlap most of the melted region and align the crystal growth direction within the layer (Fig. 1a). Furthermore, rotating the scanning direction 90° clockwise for each layer makes the crystal growth direction spiral (Fig. 1b). Only the crystal with the preferred growth direction, i.e., [001] for face-centered cubic (FCC), can continue to grow, resulting in SX growth.

In a previous study [24], the μ-helix method was applied to the laser PBF (PBF-LB) processing of 316 stainless steel specimens. SX growth was successfully achieved using a conventional Gaussian beam, as shown in Fig. 1c. Moreover, the deeper melt pool of the PBF-LB process resulted in higher growth-direction selectivity in the building direction compared with that in the PBF-LB with a top hat profile beam and the electron-beam PBF (PBF-EB) process. However, inhomogeneities were present in the crystal-orientation and solute-element distributions: polycrystalline regions were formed at the edges of the built part, and strong solute-element segregation occurred between the interdendritic regions (Fig. 1d1–1d2). These inhomogeneities must be eliminated to produce SXs with the required mechanical properties. Furthermore, solute-segregated regions exhibit reduced solidus temperatures and abnormal precipitation behavior [25]. Heat treatment must be conducted with consideration of the phase stability of the solute segregation regions to eliminate elementally inhomogeneous regions.

This study examines the impact of thermal annealing on the crystal orientation and elemental distribution of μ-helix scanning fabricated SX parts of the γ'-precipitation hardened Ni-based superalloy IN738LC. This alloy operates at a higher temperature (930 °C) compared to weldable Ni-based superalloys such as IN718 (770 °C) and Hastelloy-X (720 °C), which are currently employed in AM [26]. The as-fabricated SX part exhibits polycrystalline grains at its edges and solute segregation within the interdendritic regions. Additionally, non-equilibrium precipitates are present in the solute-segregated regions. The influence of heat treatment on microstructural evolution was examined, demonstrating that appropriate heat treatment can concurrently eliminate solute segregation and crystalline inhomogeneity.

2. Methods

2.1. SX fabrication experiment

IN738LC blocks with dimensions of 10 mm × 10 mm × 15 mm were fabricated using a PBF-LB machine (EOS M290) with μ-helix scanning, which rotates the raster direction clockwise by 90° (Fig. 1a). We used the EOS NickelAlloy IN738 powder, produced by VIGA gas atomization. Table 1 lists the alloy composition of the IN738LC powder. The laser power (P), scanning speed (V), layer thickness, and scanning line spacing (d) were 300 W, 1000 mm s^{-1}, 50 μm, and 30 μm, respectively. These parameters were determined based on our previous study of 316 L stainless steel [24], followed by a series of trial builds on the Ni-based alloy to optimize the conditions for obtaining the SX part. The melting and solidification behaviors during laser irradiation were monitored in-process using an EOSTATE MeltPool Monitoring system.

To investigate the effects of thermal annealing on the crystal orientations and microstructures, the fabricated SX samples were cut into plates with dimensions of 5 mm × 5 mm × 1 mm using an electrical discharge machine (Tainatec, DKV7732), and thermally annealed and cooled to room temperature under vacuum (<10 Pa) in the vacuum furnace (FULL-TECH FT-1650-60R). The heat treatment temperatures were 1000, 1100, 1200, and 1300 °C, which are close to the solution temperatures of carbides and the γ' phase of the IN738LC alloy (1120 °C [27] and 1235 °C [28], respectively).

The fabricated parts were etched in a nitrate etching solution composed of 31 mL HNO_3, 6 mL HF, and 63 mL H_2O at room temperature for 10 min to examine the microstructure in the melt regions. The cross-sections of the as-fabricated and annealed samples were observed using field-emission scanning electron microscopy (FE-SEM; JEOL JIB-4610F), and the crystal orientation and elemental distributions were analyzed using an FE-SEM equipped with an EBSD detector (Oxford Instruments NordlysMax^3) and an energy dispersive X-ray spectroscopy (EDS) analyzer (Oxford Instruments X-Max^N 20), respectively. The samples were also analyzed using X-ray diffraction (XRD; Rigaku SmartLab SE) to evaluate the precipitation phases. The Cu Kα source was used, and the scanning range was 20°–90° with a step size of 0.01°.

2.2. MPF simulation

Two-dimensional multi-phase-field (MPF) simulations were performed using Microstructure Evolution Simulation Software (MICRESS) [29–33] with the TQ-Interface for Thermo-Calc [34]. Notably, as the solidification growth rate increases, the segregation coefficients

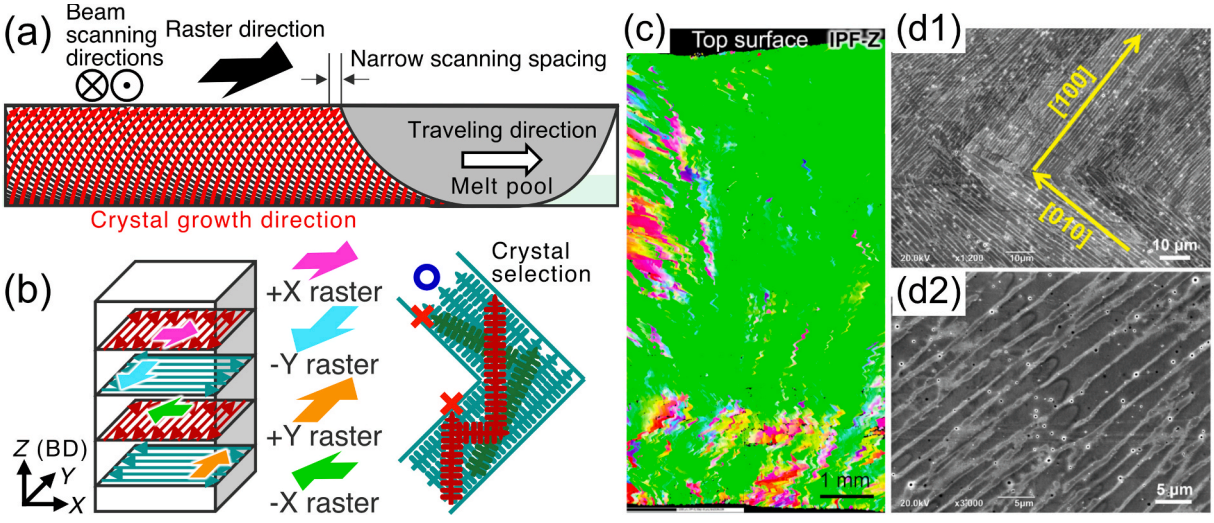

Fig. 1. (a,b) Schematic of the μ-helix scanning strategy. (c) SEM-EBSD IPF-Z map and (d) SEM-SEI images of the YZ cross-section of the PBF-LBed 316ss SX part [24].

Table 1
Composition of the IN738LC powder (mass%).

Ni	Al	Co	Cr	Fe	Mo	Nb	Ta	Ti	W	Zr	B	C	O	N	Si	S	P
Bal.	3.44	8.64	16.18	3.80	1.76	0.87	1.75	3.52	2.66	0.07	0.004	0.13	0.014	0.010	0.03	0.002	<0.008

approach 1, and fluctuations at the solid/liquid interface are suppressed by interfacial tension. Additionally, at the solid/liquid interface, growth with a cellular morphology occurs at a solidification rate above the absolute stability according to limit, R_{as}, as predicted by the Mullins-Sekerka theory [35]: $R_{AS} = (\Delta T_0\ D_L)/(k\ \Gamma)$, where ΔT_0, D_L, k, and Γ are the difference between the liquidus and solidus temperatures, equilibrium partition coefficient, solute diffusivity in the liquid, and the Gibbs-Thomson coefficient, respectively. We proposed in the previous study [25] that the absolute stability limit, R_{AS}, could be used as an indicator to evaluate the degree of deviation from equilibrium. We demonstrate that the microstructure formation in the PBF-LB process of the Ni-based superalloy with the large ΔT_0 (134 K), which directly determines $R_{AS,}$ can be reproduced using the conventional PF model [25]. Table 2 shows the simplified composition for the PF simulation, and ΔT_0 is evaluated as 103 K using Thermo-Calc software. Thus, we used the conventional MPF model also in this study. The Gibbs free energy and diffusion coefficient of the system were calculated using the TCNI10 thermodynamic database [36] and MOBNI5 mobility database [37], respectively. The MPF simulations assumed a two-phase system consisting of liquid and FCC phases only. The simulation domain was 5 μm × 100 μm, and the grid size (Δx) and interface width were set to 0.025 and 0.1 μm, respectively. The interfacial mobility between the solid and liquid phases was set to 1.0×10^{-8} m^4 J^{-1} s^{-1}. Initially, one crystalline nucleus with the [100] crystal orientation was placed at the bottom left of the simulation domain, with the liquid phase occupying the remainder of the domain. The model was solidified under the conditions of a cooling rate of 1.0×10^6 K s^{-1} and a temperature gradient of 1.0×10^7 K m^{-1}, which are typical of conditions encountered in the PBF of Ni-based superalloys [25,38]. The crystal orientation and elemental distributions of the solidified model were examined.

3. Results and discussion

3.1. Crystal orientation and microstructure of the as-fabricated SX

Fig. 2a1–a3 show EBSD-IPF maps of the cross-sections of the specimen fabricated using μ-helix scanning, and Fig. 2b shows an EBSD grain boundary map with a misorientation threshold of 7° indicated by red lines. The crystal orientation of the fabricated specimen could be divided into three regions. In Region I, the crystals near both ends of the fabricated specimen grew in an inclined direction with a polycrystalline microstructure. In Region II, the crystals grew parallel to the building direction as they moved from Region I to the +Y direction, and the crystal grains were oriented mainly along <100> in the X-, Y-, and Z-directions. In Region III, the crystal orientation was the highest, and the SX was oriented toward <100> in the *X*-direction and <110> in the Y- and Z-directions (BD). Magnified EBSD-IPF maps of Region III are shown in Fig. 2c1–c3. The (100) orientation distribution function (ODF) is shown in Fig. 2c4. The crystal structure was highly oriented, indicating that the SX could be fabricated using PBF-LB with μ-helix scanning. We attribute the polycrystalline microstructure near the edge region to non-uniform melt-pool size arising from differences in heat accumulation during processing.

Fig. 3a and 3b show the SEM cross-sectional images of the XZ and YZ planes of the built part of the SX. There are differences in melt pool shapes across scanning directions: the melt pools formed by the ±x scans are uniform, with a depth of 313 μm. In contrast, the shallower melt pools formed by the ±y scans have a different depth. The difference in melting and solidification behavior during y-direction scanning was detected by in-process monitoring. Fig. 3c shows the intensities of the on-axis light signals obtained using the in-process monitoring system during the X and Y raster layer fabrications. The intensities were almost the same during the Y raster (±x scans), but the intensity during the −y scan was greater than that in the +y scan. However, the light intensities detected in the −y scan were approximately two times greater than those in the +y scan during the X raster fabrication, and the lower intensity detected during the +y scan was roughly the same as that during the +x scan. These results indicate that the in-process monitoring system can detect differences in the melting and solidification behavior. The anisotropy in the melt pool shapes along the x- and y-directions may have been caused by the gas-flow effect, even though the laser scanning was isotropic in the x- and y-directions [24,39], because the PBF machine used argon as a shielding gas. The argon gas flows directly above the build plate in the −y direction and sweeps away the fumes generated by the laser irradiation in the −y direction. This flow blocks laser irradiation of the powder bed and reduces the laser intensity during the −y scan. The gas-flow effect is also discussed by combining experimental observations of the formed melt pool with computational thermal-fluid dynamics simulations, including the gas phase [39].

Fig. 3d–3f show schematics of the stacking layers in the narrow-spacing scanning. During a Y raster scan, all the regions melted by the X raster scan are overlapped by the scan with a narrow spacing (Fig. 3e). Consequently, only crystal grains grown perpendicular to the melt pool boundary remain, and the crystal growth direction is aligned within the layer. The temperature gradient direction of almost the entire region was tilted by approximately 45° relative to the building direction, i.e., the [110] direction relative to the X and Z directions, which is in agreement with the crystal orientation of the experimentally fabricated SX part (Fig. 2a–2c). The melt pool depth of the Y-raster layer was larger than that of the X-raster layer. Therefore, the layers formed by ±X raster scans were remelted during the ±Y raster scans (Fig. 3f), and the ±Y raster scans determined the crystal growth direction. Furthermore, only crystals oriented at ±45° were selected for growth by changing the raster directions; thus, the built part formed an SX. In PBF-LB with Gaussian-shaped beam, deep melt pools are formed. It has previously been proposed that specific crystal orientations such as (100) and (110) planes can be fabricated by controlling the laser scanning strategy [11–14]. Furthermore, in our previous study on the SX fabrication of single-crystal 316 L steel using the μ-Helix scanning, we reported the hypothesis that gas flow influences the process, causing ±Y raster scanning (±x scanning) to become the dominant growth direction and thereby inducing a (110) crystal orientation. In the present study, we successfully employed in-process monitoring to directly observe the differences in melting behavior, yielding results that support the proposed mechanism for the formation of crystal orientation.

Fig. 4a and 4b show a magnified IPF-Z map and the corresponding

Table 2
Composition used in the PF simulation (mass%).

Ni	Al	Co	Cr	Fe	Mo	Nb	Ta	Ti	W	B	C
Bal.	3.44	8.64	16.18	3.80	1.76	0.87	1.75	3.52	2.66	0.004	0.13

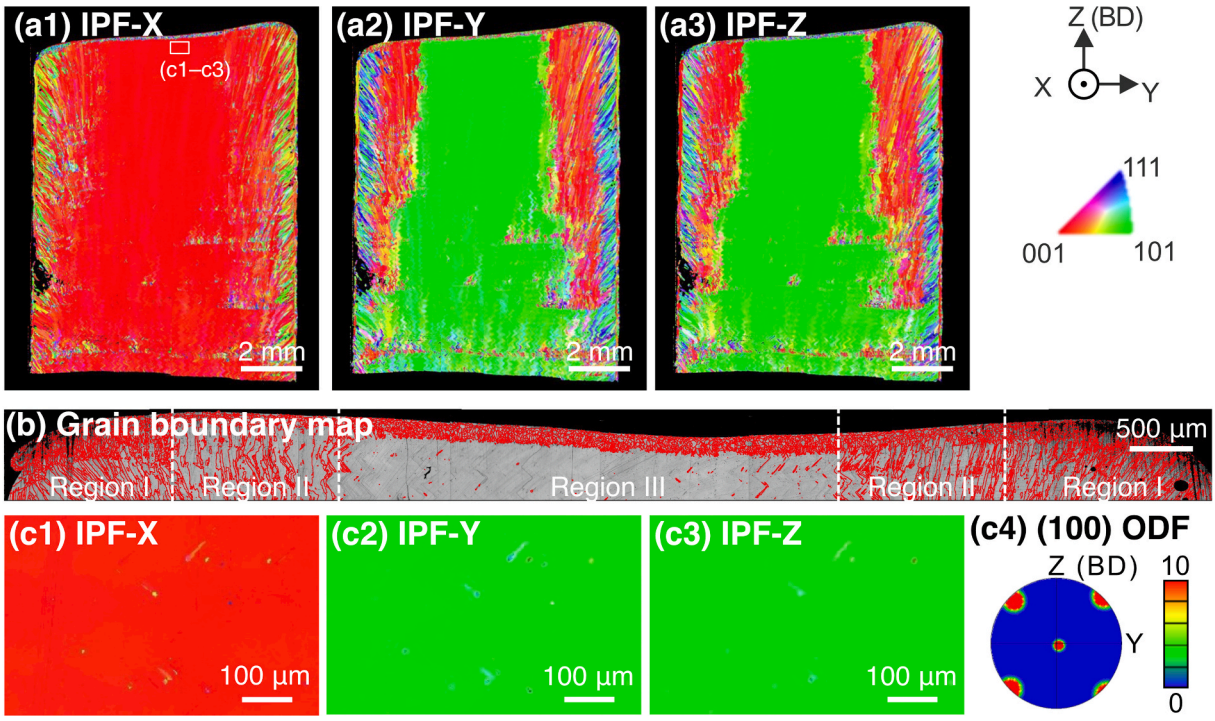

Fig. 2. (a1)–(a3) EBSD inverse pole figure (IPF) maps. (b) EBSD grain boundary map with misorientation threshold of 7° indicated by red colored lines. (c1)–(c3) Magnified maps indicated by the rectangle in a1. (c4) (100) orientation distribution function (ODF) of the pole figures from the EBSD measurements in c1–c3. (For interpretation of the references to colour in this figure legend, the reader is referred to the web version of this article.)

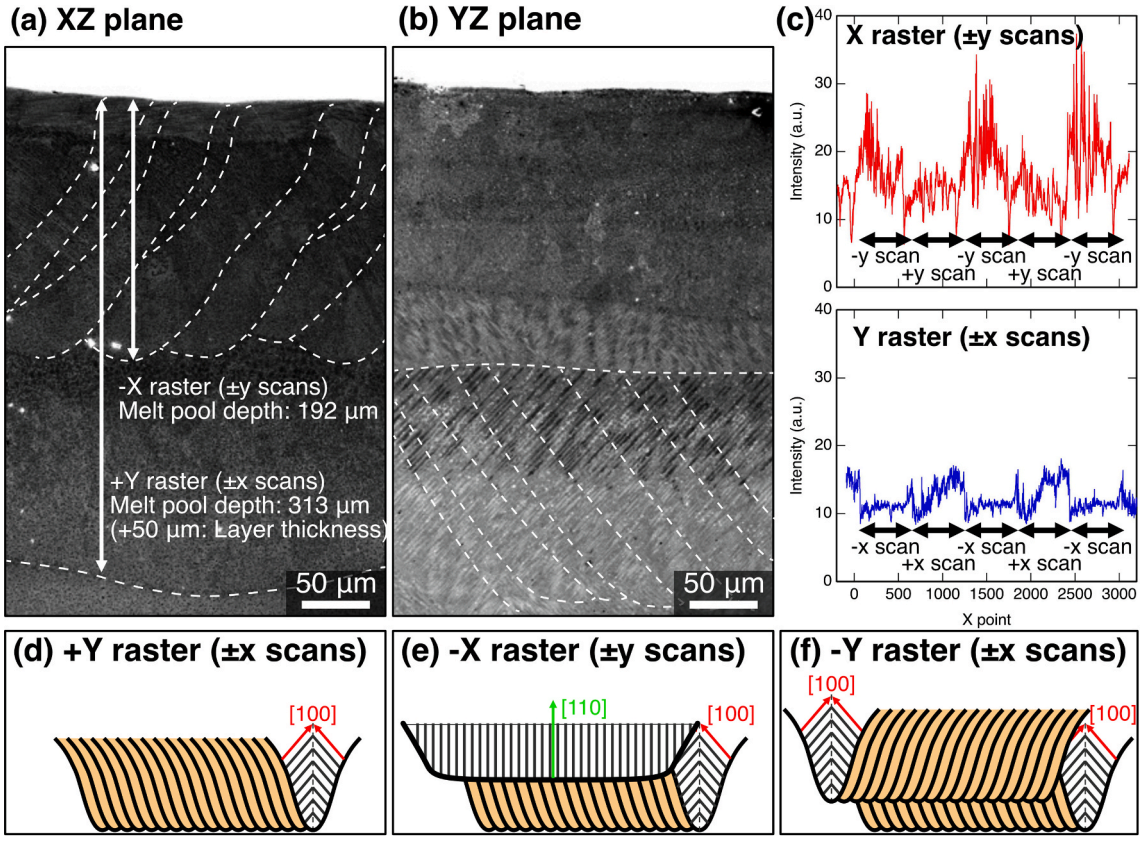

Fig. 3. SEM cross-sectional images of the (a) XZ plane and (b) YZ plane of the SX built part. (c) Intensity profiles obtained by the in-situ monitoring system during X and Y raster scans, (d)–(f) Schematic illustrations of the stacking layers in indicating the shape of melt-pools (thick lines), the direction of crystal growth (thin lines), and remaining solid part (light orange). (For interpretation of the references to colour in this figure legend, the reader is referred to the web version of this article.)

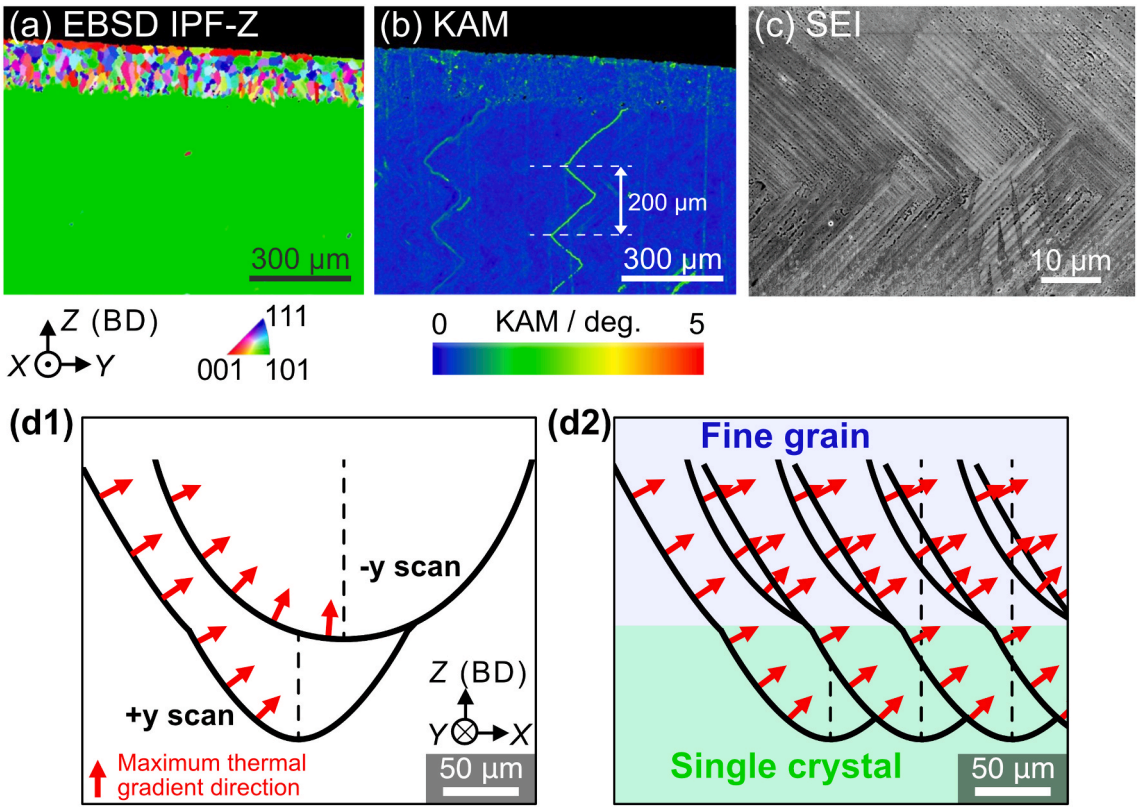

Fig. 4. (a) Magnified IPF-Z map of the top of the SX region (Region III) and (b) the corresponding kernel average misorientation (KAM) map. (c) SEM secondary electron image (SEI) of the SX region (Region III). (d1, d2) Schematic illustration of the mechanism for fine-grain formation near the surface region.

kernel average misorientation (KAM) maps of the top of the SX area in region III, respectively. The KAM map shows that zigzag-shaped high-strain areas form in Region III with a period of approximately 200 μm, corresponding to four times the layer thickness. A zigzag pattern can also be observed in the SEM cross-sectional secondary electron image (SEI) shown in Fig. 4c. During μ-helix scanning, the crystal growth direction within the layer is aligned with the narrow scanning line spacing (Fig. 1a). Furthermore, the crystals to be grown are selected by rotating the scanning direction 90° clockwise for each layer (Fig. 1b) and making the crystal growth direction spiral. The formation of these stray grains (Fig. 4b) indicates that the selection of crystal grains occurs during layer stacking. However, crystals with slightly different orientations survived grain selection by μ-helix scanning, and thus very thin crystals with different orientations were introduced.

It is worth noting that fine polycrystalline grains with a diameter of approximately 20 μm can be observed in the surface regions of the SX part (Fig. 4a). The fine-grain microstructure is formed in the region where the deep and shallow melt pool formations are repeated (Fig. 3a). Fig. 4d1–4d2 show schematic illustrations of the microstructural formation. The crystal growth direction changed drastically at the melt pool boundary, which possibly prevented epitaxial growth of the crystal grains, and thus a polycrystalline microstructure was formed. However, the thickness of the surface polycrystalline layer is approximately 190 μm, which is shallower compared to the melt pool depth of 313 μm formed during ±Y rastering (±x scanning), considering the layer thickness of 50 μm. Consequently, this polycrystalline layer is suggested not to influence the crystal orientation of the bulk region, as it undergoes remelting during the formation of the subsequent layer.

Fig. 5a shows the XRD profile of the as-built sample. The peaks can be identified as FCC, γ' intermetallic, and various carbide and boride phases. The carbide and boride phases could not be definitively identified as specific phases such as *M*C, MB_2, or M_3B_2 because multiple candidates were present, and the XRD peaks could not be conclusively assigned to a single phase. Conversely, the precipitate behavior differs from that predicted by the equilibrium thermodynamic calculations, as shown in Fig. 5b. It is well-known that strong solute-element segregation occurs in the micron or submicron-sized fine interdendritic regions due to the rapid cooling rate (up to 10^8 K s^{-1}) unique to the PBF-LB process [25,40–42]. Moreover, this strong solute-element segregation affects the precipitation behavior [25,43]. Notably, this precipitation is involved in hot cracking in PBF-LB fabricated parts [43], and understanding the solute-element segregation is essential for producing reliable PBF-LB fabricated parts while suppressing cracks. The SX part also contains strong solute-segregation in the entire regions, as shown in the SEM SEI image and the corresponding EDS maps in Fig. 5c and 5d. The EDS results show the solute-element segregation of Ti, Nb, and Mo occurring at the interdendritic regions. This solute-element segregation behavior is expected to enhance the formation of carbides and borides. We also confirmed that there are almost no differences in the solidification cell structure between the SX and polycrystalline regions.

To determine the stability of the strong solute-element segregation, an MPF directional solidification simulation was performed. Fig. 6a and 6b show the MPF models during solidification, colored by phase (Fig. 6a) and Ti concentration (Fig. 6b). Dendrites grew parallel to the heat-flow direction, and all the computational domains after solidification were in the FCC phase. Strong solute-element segregation can be observed in the interdendritic regions. Fig. 6c and 6d show the concentration profiles along the line perpendicular to the growth direction at the center of the completely solidified model. B, C, Nb, Mo, Ti, Ta, and W segregated and were concentrated in the interdendritic regions, whereas the concentrations of Al, Cr, Co, and Fe in the interdendritic regions were lower. Notably, B segregated in the interdendritic regions, but the segregation behavior was inhomogeneous across the various segregated regions. This solute segregation tendency agrees with the experimental results (Fig. 5c and d). The most pronounced segregation occurred for Ti. In contrast, for C, the ratio of the segregated amount to

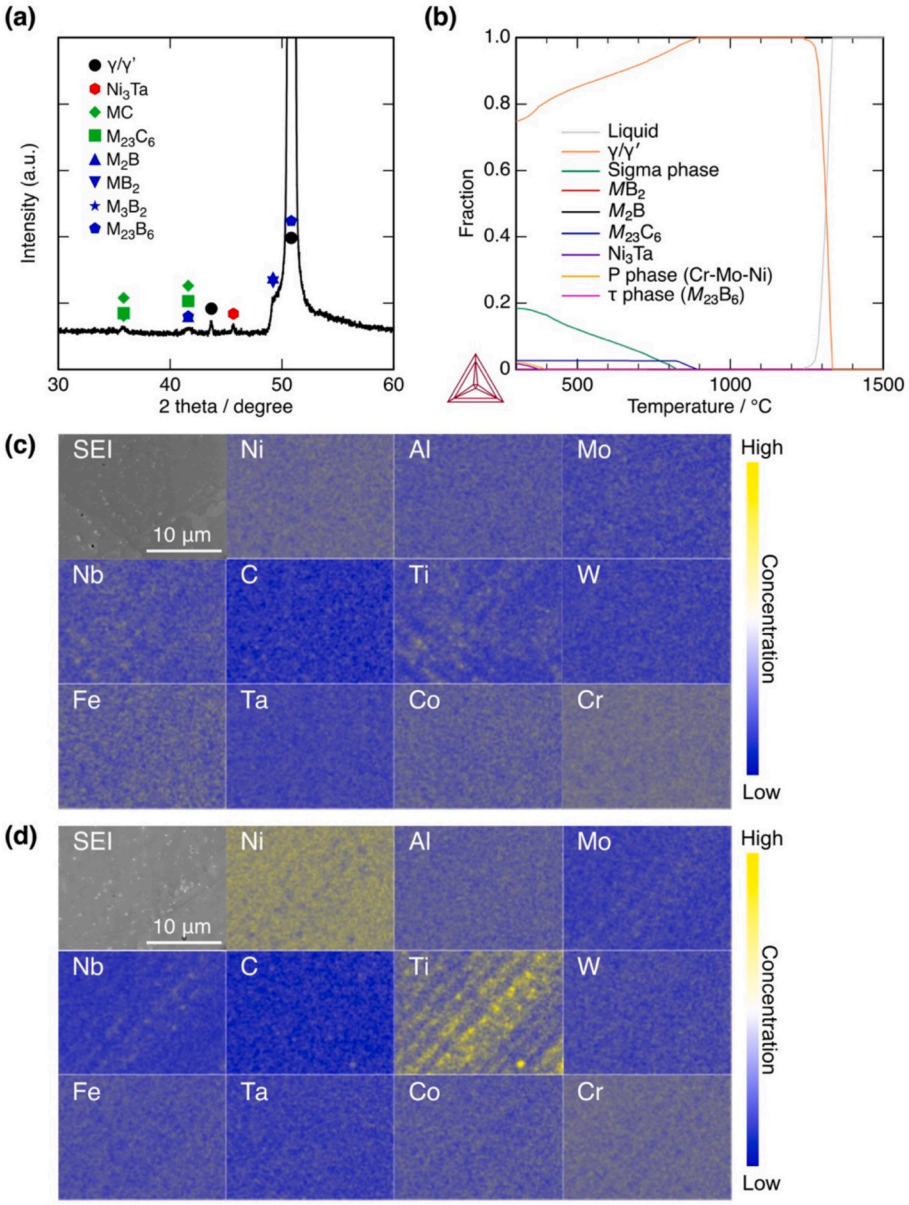

Fig. 5. (a) XRD profile of the as-built sample. (b) Volume fraction of the constituent phases in thermodynamic equilibrium calculated for the alloy composition as a function of temperature. (c,d) SEM SEI and the corresponding SEM-EDS elemental distributions of the Polycrystalline (Region I) and SX regions (Region III).

the alloy composition was remarkable.

The stability of the solute-element segregation and its effects on precipitate formation were considered based on the thermodynamic equilibrium calculations. Fig. 6e and f show the chemical potentials and diffusion coefficients, respectively, of the solute elements for the FCC phase at 800 °C calculated using the composition of the solidified model (Fig. 6c and d). All the elements exhibited non-uniform distribution of chemical potentials and diffusion coefficients along the perpendicular direction. It is suggested that the segregation can be relaxed easily by heat treatment. In contrast, solute-element segregation is predicted to significantly affect the formation behavior of the precipitate phases; Fig. 7 shows the fractions of the precipitate phases at 800 °C obtained by equilibrium calculations using the concentration profiles of the solidified model. The approximate compositions of the precipitate phases σ, $M_{23}C_6$, M_2B, and MB_2 phases are $Cr_{0.33}Ni_{0.1}Co_{0.1}Fe_{0.05}Mo_{0.05}$, $(Cr_{21}Mo_2)C_6$, $(Cr_{1.33}Mo_{0.67})B$, and TiB_2, respectively, and these fractions are increased significantly in the segregated region. Thus, solute-element segregation is suggested to promote the formation of non-equilibrium precipitates.

3.2. Improved quality of the PBF-LB fabricated SX through optimized thermal annealing

Thermal annealing experiments were conducted to eliminate the polycrystalline edge regions and increase the quality of the PBF-LB fabricated SX. Fig. 8a1, 8b1, and 8c1 show the EBSD IPF and KAM maps of the SX parts subjected to heat treatments at 1000 °C, 1200 °C, and 1300 °C for 1 h, respectively. The SX regions remained after annealing at 1000 °C (Fig. 8a1). Moreover, the zigzag-patterned high-strain regions can also be observed in the KAM maps. In contrast, polycrystallization occurred in the polycrystalline and SX regions annealed at 1300 °C (Fig. 8c1), and equiaxed polycrystalline grains with diameters of approximately 100–200 μm were formed. The width of the polycrystalline region could only be decreased by heat treatment at 1200 °C (Fig. 8b1) compared with the width of the as-fabricated sample (Fig. 2a1–2a3). Therefore, the SX parts were subjected to longer

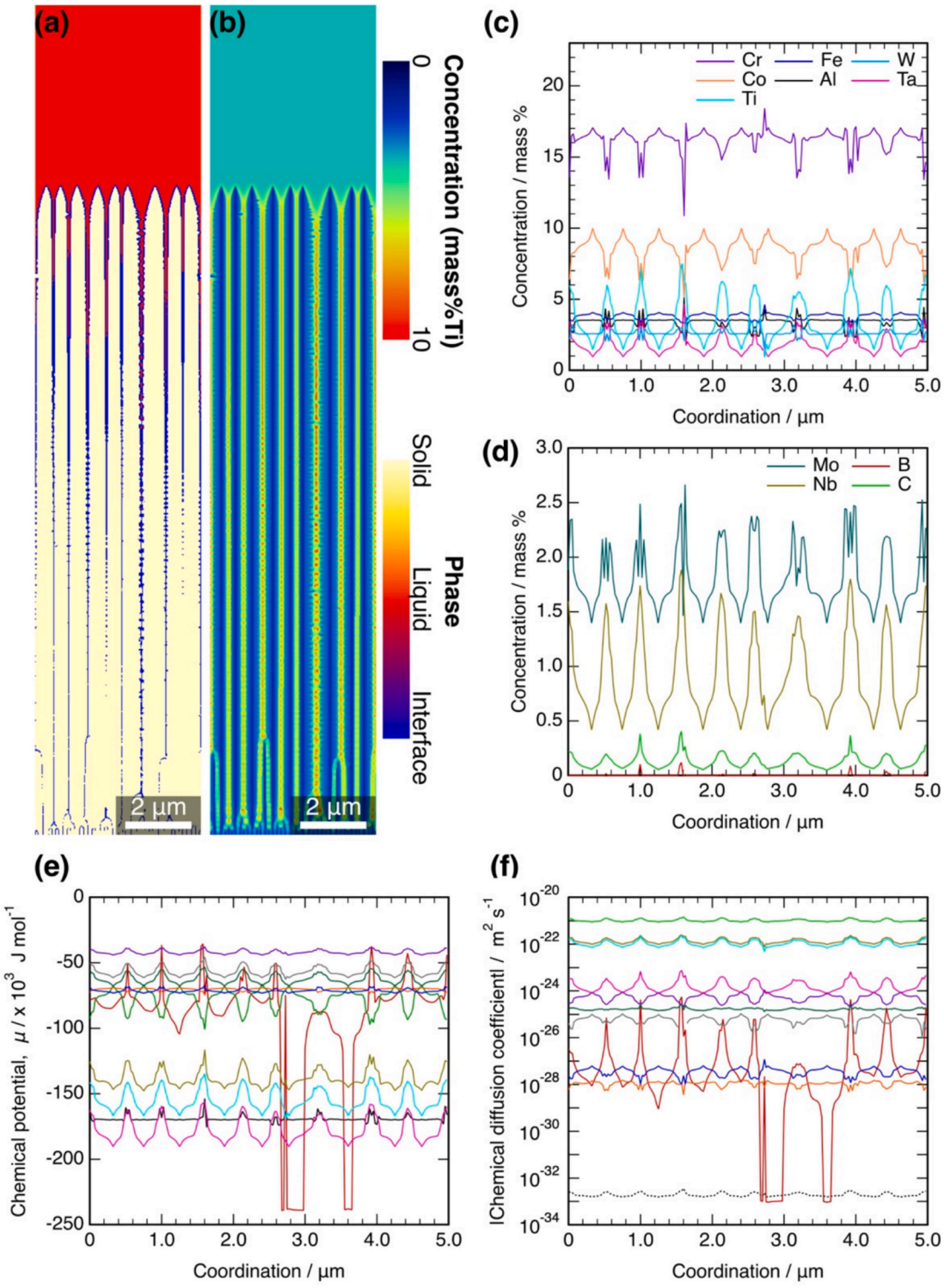

Fig. 6. MPF solidified models colored by (a) phase and (b) Ti concentration. (c), (d) Concentration line profiles at the center of the domain. (e) The corresponding chemical potentials of each solute element and (f) chemical diffusion coefficients at 800 °C.

annealing durations, i.e., 10 h and 24 h at 1200 °C, and the EBSD and corresponding KAM maps of the annealed samples are shown in Fig. 8b2 and 8b3. The polycrystalline regions, Regions I and II, were reduced in size by the thermal treatment. Thus, these results demonstrate that the SX region can be grown using optimized thermal annealing. We consider the driving force for single-crystallization during annealing is twofold: first, the cellular structure present in the as-built part makes the initial microstructure thermodynamically unstable; second, decreasing grain boundaries further reduces the system's total free energy. We propose that further optimized thermal processing can diminish the remaining polycrystalline regions, as these areas are less stable than single-crystal region.

We suggest that the polycrystallization occurs via a melting and crystallization mechanism promoted by the solute segregations. Fig. 9a shows local solidus and liquidus temperatures obtained from equilibrium calculations using the concentration profiles of the fully solidified

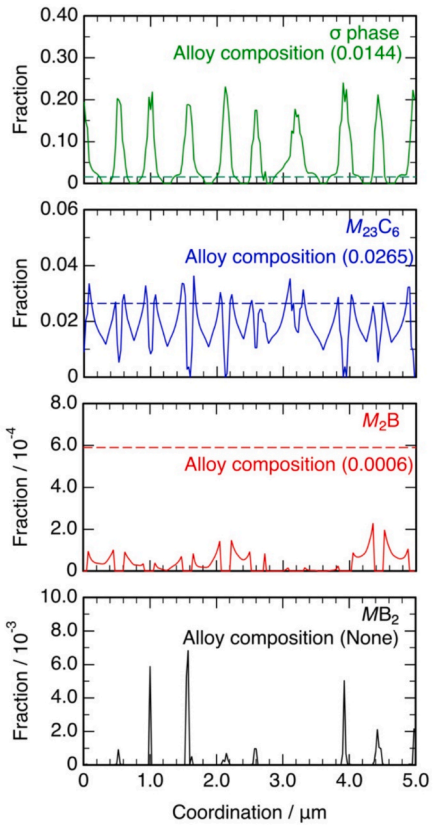

Fig. 7. Volume fractions of the precipitate phases at 800 °C obtained through equilibrium calculations using the concentration profiles of the MPF solidified model.

MPF model (Fig. 6). The temperatures depend on local composition, and the solidus temperature decreases and the liquidus temperature increases in the segregation region, compared with the solidus temperature of 1242 °C and the liquidus temperature of 1335 °C for the alloy composition. The volume fraction of the liquid phase at 1300 °C is higher in almost all regions, as shown in Fig. 9b. The polycrystallization under the thermal treatment at 1300 °C (Fig. 8c1) is suggested to occur via liquid-phase formation enhanced by the solute segregations, as schematically illustrated in Fig. 9c1–c3; a PBF-LBed SX part contains solute segregated regions (Fig. 9c1) and is partly melted after being subjected to 1300 °C (Fig. 9c2). Subsequently, the liquid regions crystallize and grow during cooling (Fig. 9c3). As a result, the polycrystalline microstructure is supposed to be formed (Fig. 8c). Notably, the as-fabricated SX part in this study contains the geometrically necessary dislocations (GNDs), as observed in the KAM maps (Fig. 4b). Moreover, PBF-fabricated alloy parts have been reported to contain high-density dislocations at the cell interfaces [4,44]. The dislocations are supposed to be present in the SX sample. These defects are suggested to enhance atomic migration and promote the grain growth during heat treatment at 1300 °C (Fig. 8c).

Fig. 10a1–10a3 show the SEM-SEI and the corresponding EDS Ti distribution of the sample treated at 1000 °C, 1200 °C, and 1300 °C for 1 h, respectively. No segregation of solute elements was observed after the heat treatments. These results indicate that segregation in the SX samples can be eliminated by thermal annealing at the optimized temperature for single crystallization. This relaxation behavior is consistent with simulation predictions (Fig. 6e and 6f), which indicate that segregation is a non-equilibrium phenomenon. In contrast, precipitate behavior depends on the annealing temperature: the precipitates are eliminated when annealed at 1300 °C, whereas they remain present in the sample thermally treated at and below 1200 °C, even above the solution temperature for IN738LC [27]. The XRD patterns shown in Fig. 10b indicate that the precipitation phases increased with annealing at 1200 °C compared to the as-built sample. Fig. 10c shows the fractions of the precipitate phases at 1200 °C obtained through equilibrium calculations using the concentration profiles of the fully solidified MPF

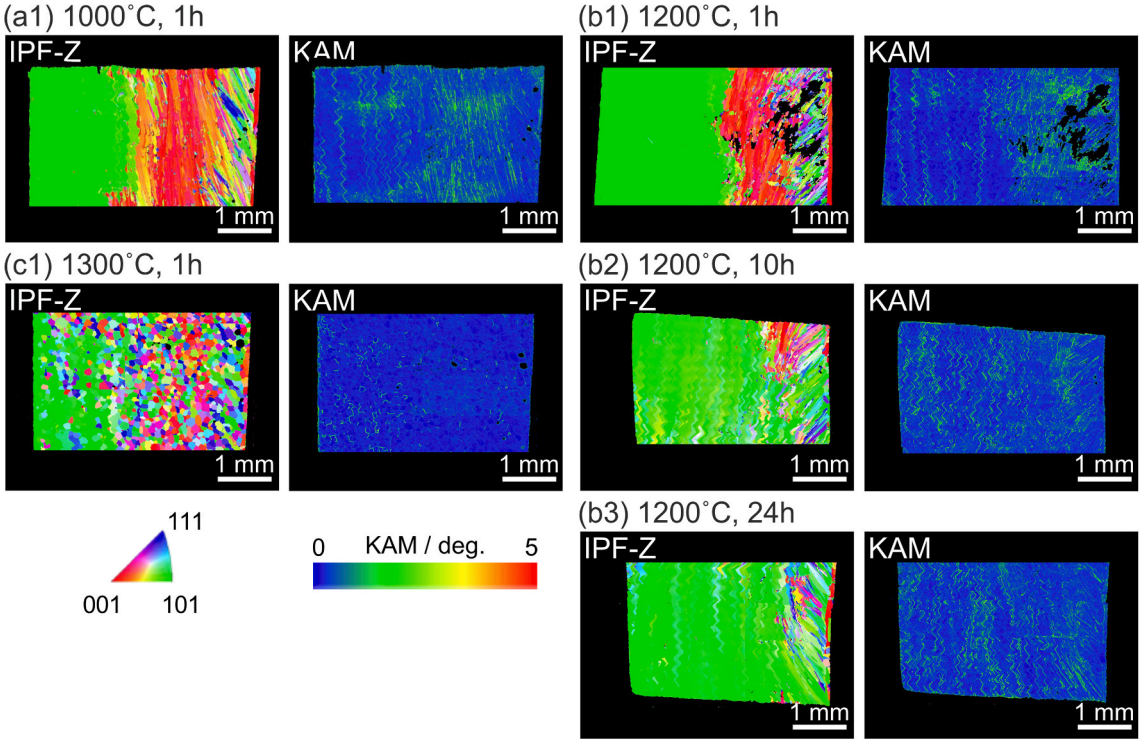

Fig. 8. EBSD inverse pole figure (IPF) orientation maps and the corresponding KAM maps of SX samples subjected to thermal treatments: (a1) 1000 °C for 1 h, (b1) 1200 °C for 1 h, (b2) 1200 °C for 10 h, (b3) 1200 °C for 24 h, (c1) 1300 °C for 1 h.

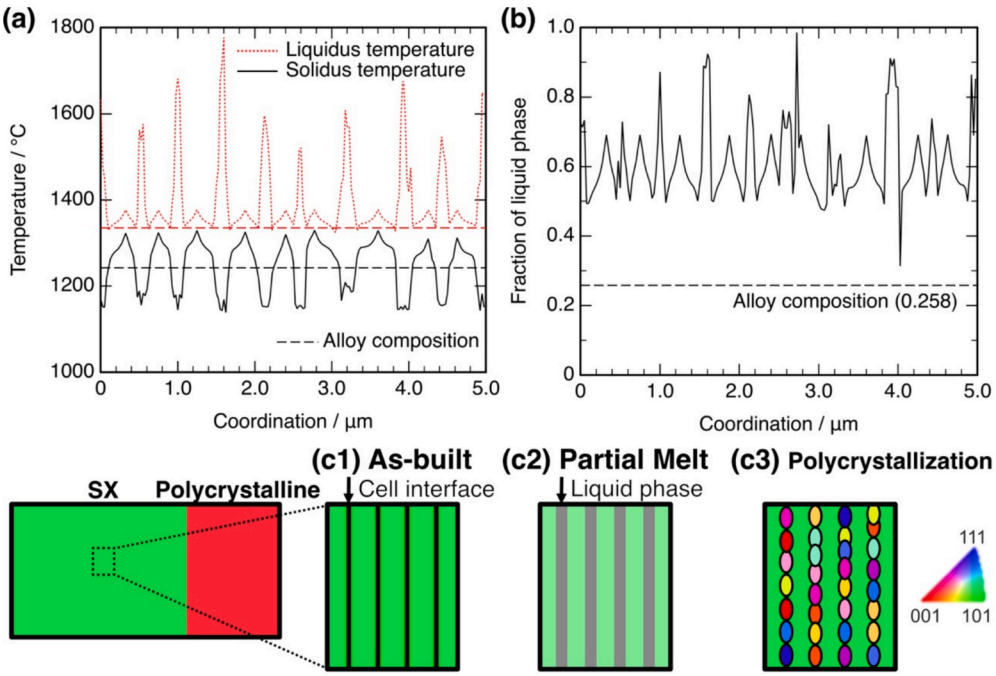

Fig. 9. (a) Solidus and liquidus temperatures and (b) fractions of liquid phase at 1300 °C obtained through equilibrium calculations using the concentration profiles of the fully solidified MPF model. (c1–c3) Schematic illustrations of polycrystallization under the thermal treatment at 1300 °C; (c1) before annealing, (c2) during annealing at 1300 °C, and (c3) during cooling after annealing.

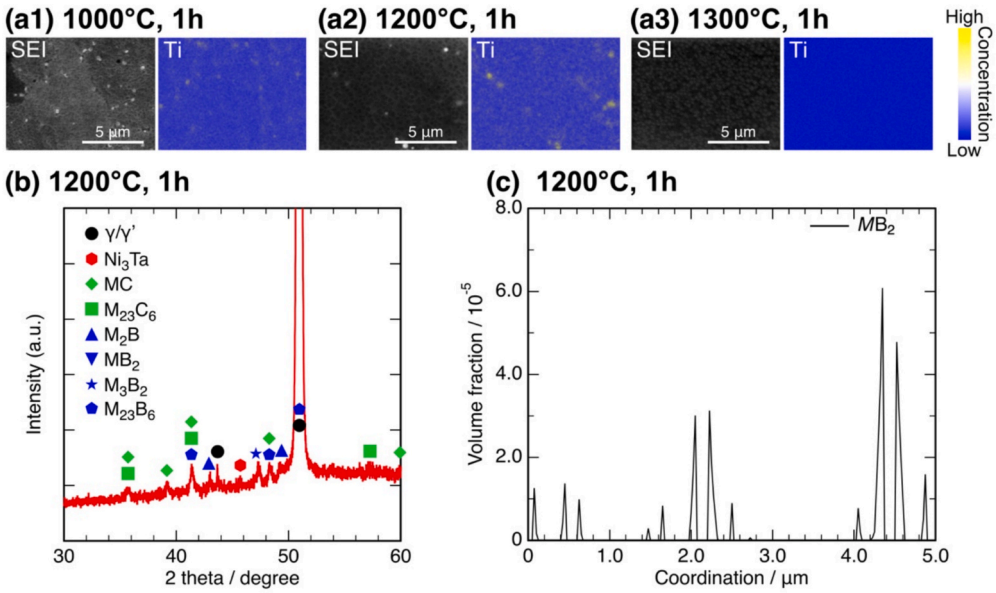

Fig. 10. (a1–a3) SEM SEI and SEM-EDS Ti elemental distribution maps of the SX part subjected to thermal treatment at 1000 °C, 1200 °C, and 1300 °C for 1 h. (b) XRD profile of the sample annealed at 1200 °C for 1 h. (c) Volume fractions of the precipitate phases at 1200 °C obtained through equilibrium calculations using the concentration profiles of the fully solidified MPF model.

model (Fig. 6). The MB_2 phase, approximately TiB_2, was stable even above the solution temperatures, suggesting that the precipitates, whose formation is promoted by solute element segregation, are difficult to eliminate.

Table 3
Summary of the effects of thermal treatments on the PBFed SX samples.

Sample condition	As-built	1000 °C	1200 °C	1300 °C
Texture	SX + Polycrystalline	SX + Polycrystalline	SX	Polycrystalline
Segregation and precipitation in SX	Segregations + Precipitates	Precipitates	Precipitates	–

We summarize the obtained results in Table 3 to provide guidelines for optimal thermal treatment to obtain a fully SX Ni-based superalloy using the PBF-LB process. The as-built sample fabricated by PBF-LB was SX in the central part, while polycrystalline microstructures were present in the edge regions. Solute element segregations and the associated precipitation of carbides and borides were observed within the crystal grains. The changes in texture varied with annealing temperature: Heat treatment below 1100 °C showed little change. Heat treatment at 1200 °C expanded the single-crystal region toward the fully SX. Heat treatment at 1300 °C resulted in recrystallization. This recrystallization is suggested to result from local melting of segregated regions with low melting points. These heat treatments also resulted in relaxation of solute segregation. Meanwhile, the precipitates formed in the segregated areas remained even after heat treatment at 1200 °C, which is higher than the typical solution temperature. We propose an optimized heat treatment condition based on the findings of this study. First, the as-built part produced by PBF-LB are heat-treated at 1200 °C to promote single crystallization and relax solute segregation. Then, the precipitates are solution-treated at a temperature just below the solidus temperature. In this study, although the target geometry is a simple cubic, we demonstrate that by controlling the scanning strategy, heat accumulation can be managed to promote single-crystal formation even in more complex components. We also consider one of the key contributions of this work to be that the polycrystalline region near the edge can be reduced through heat treatment. These advantages would become even more pronounced when applied to more complex structures. On the other hand, polycrystalline regions are present along the edges in the single-crystal materials fabricated in this study (Regions I and II). Furthermore, stray grains are observed within the single-crystal region (Region III). Achieving a more uniform crystal orientation in the as-fabricated state is expected by using a shaped beam, a technology that has garnered significant attention in recent years, and the study is currently underway.

Avoiding hot cracks is required to produce reliable PBF-LB fabricated Ni-based superalloy parts, and crack susceptibility is related to solute-element segregation and accompanying precipitation [44]. In fact, a crack was visible in the edge region of the PBF-LB fabricated SX part (Fig. 2a1–a3), which exhibited strong inhomogeneity in the elemental distributions (Fig. 5b). It is necessary to solidify the part with no solute-element segregation to suppress hot cracking during building. Currently, control of rapid solidification conditions in the PBF process has been proposed for use to suppress solute-element segregation [6]. As described in the Method section, interfacial tension suppresses fluctuations at the solid/liquid interface during rapid solidification beyond the R_{AS}. It can be suggested that an alloy designed to have a low R_{AS} can be solidified without cellular morphology, yielding a crack-free SX part. The design of Ni-based superalloys with low R_{AS} using the Bayes optimization technique is currently underway.

4. Conclusion

This study demonstrated that PBF-LB SX growth can be achieved by applying the μ-helix scanning strategy to the γ′ precipitation-strengthened Ni-based superalloy IN738LC. The crystal orientation of the SX regions was <100> in the X-direction and <110> in the Y- and Z-directions. This was explained by the difference in the melt pool shapes formed by ±y scans, which could be detected by the in-process melt pool monitoring system. The SX region was expanded by optimal thermal annealing. Additionally, heat treatment could eliminate the inhomogeneity in the elemental distributions formed during rapid cooling. This study exhibits a pathway toward fully single-crystallization of Ni-based superalloys, which can assist in the development of advanced high-temperature materials for a broad range of aerospace and energy applications.

Funding sources

This work was partly supported by the Cabinet Office, Government of Japan, Cross-ministerial Strategic Innovation Promotion Program (SIP), "Materials Integration for Revolutionary Design System of Structural Materials," (funding agency: The Japan Science and Technology Agency), by the JSPS KAKENHI Grant-in-Aid for Transformative Research Areas (A) "Creation of Materials by Super Thermal Field: Neo-3D Printing by Manipulating Atomic Arrangement through Giant Potential Gradient" [grant numbers: 21H05018 and 21H05193], and by CREST Nanomechanics: "Elucidation of Macroscale Mechanical Properties based on Understanding Nanoscale Dynamics for Innovative Mechanical Materials" [grant number: JPMJCR2194] from the Japan Science and Technology Agency (JST).

CRediT authorship contribution statement

Masayuki Okugawa: Writing – review & editing, Writing – original draft, Visualization, Validation, Software, Methodology, Investigation, Formal analysis, Data curation, Conceptualization. **Kazufumi Nose:** Writing – original draft, Visualization, Validation, Software, Methodology, Investigation, Formal analysis, Data curation. **Sei Hirooka:** Visualization, Validation, Software, Methodology, Investigation, Formal analysis, Data curation. **Sukeharu Nomoto:** Writing – review & editing, Validation, Investigation. **Yuheng Liu:** Writing – review & editing, Validation, Investigation, Formal analysis. **Makoto Watanabe:** Writing – review & editing, Validation, Project administration, Funding acquisition. **Yuichiro Koizumi:** Writing – review & editing, Visualization, Validation, Supervision, Project administration, Methodology, Investigation, Funding acquisition, Formal analysis, Data curation, Conceptualization. **Takayoshi Nakano:** Writing – review & editing, Validation, Supervision, Project administration, Funding acquisition.

Declaration of competing interest

The authors declare that they have no known competing financial interests or personal relationships that could have appeared to influence the work reported in this paper.

Acknowledgements

The authors would like to thank Mr. H. Kawabata and Mr. K. Kimura for their technical support with the sample preparations.

Data availability

Data will be made available on request.

References

[1] M. Gell, D. Duhl, A.F. Giamei, The development of single crystal superalloy turbine blades, Superalloys (1980) 205–214.
[2] A. Mostafaei, R. Ghiaasiaan, I.T. Ho, S. Strayer, K.C. Chang, N. Shamsaei, S. Shao, S. Paul, A.C. Yeh, S. Tin, A.C. To, Additive manufacturing of nickel-based superalloys: a state-of-the-art review on process-structure-defect-property relationship, Prog. Mater Sci. 136 (2023) 101108, https://doi.org/10.1016/j.pmatsci.2023.101108.
[3] Y. Li, X. Liang, Y. Yu, D. Wang, F. Lin, Review on additive manufacturing of single-crystal nickel-based superalloys, Chin. J. Mech. Eng. Addit. Manuf. Front. 1 (2022) 100019, https://doi.org/10.1016/j.cjmeam.2022.100019.
[4] Y.M. Wang, T. Voisin, J.T. McKeown, J. Ye, N.P. Calta, Z. Li, Z. Zeng, Y. Zhang, W. Chen, T.T. Roehling, R.T. Ott, M.K. Santala, P.J. Depond, M.J. Matthews, A. V. Hamza, T. Zhu, Additively manufactured hierarchical stainless steels with high strength and ductility, Nat. Mater. 17 (2018) 63–71, https://doi.org/10.1038/nmat5021.
[5] J.H. Martin, B.D. Yahata, J.M. Hundley, J.A. Mayer, T.A. Schaedler, T.M. Pollock, 3D printing of high-strength aluminium alloys, Nature 549 (2017) 365–369, https://doi.org/10.1038/nature23894.
[6] Y. Koizumi, M. Okugawa, Digital twin science of metal powder bed fusion additive manufacturing: a selective review of simulations for integrated computational materials engineering and science, ISIJ Int. 62 (2022) 2183–2196, https://doi.org/10.2355/isijinternational.ISIJINT-2022-184.
[7] M. Okugawa, Y. Isono, Y. Koizumi, T. Nakano, Raking process for powder bed fusion of Ti6Al4V alloy powder analyzed by discrete element method, Mater. Trans. 64 (2023) 37–43, https://doi.org/10.2320/matertrans.MT-MLA2022010.

[8] K. Cho, K. Yamashita, T. Saito, T. Sasaki, K. Sawaizumi, M. Okugawa, Y. Koizumi, T. Mayama, T. Ishimoto, Wu. Hajime Kimizuka, T.K. Gong, S. Harjo, T. Nakano, H. Y. Yasuda, Effect of nanoscale cellular structure on the mechanical properties of Inconel 718 with unique hierarchical structure fabricated by laser powder bed fusion, Acta Mater. 303 (2026) 121696, https://doi.org/10.1016/j.actamat.2025.121696.
[9] X. Zhang, B. Mao, L. Mushongera, J. Kundin, Y. Liao, Laser powder bed fusion of titanium aluminides: an investigation on site-specific microstructure evolution mechanism, Mater. Des. 201 (2021) 109501, https://doi.org/10.1016/j.matdes.2021.109501.
[10] F. Zhang, C. Peng, T. Zhu, X. Xie, L. Zhou, Y. Li, Tailoring single-crystal-like textures in a non-weldable Ni-based superalloy by controlling overlap behavior in laser powder bed fusion, J. Mater. Process. Technol. 347 (2026) 119143, https://doi.org/10.1016/j.jmatprotec.2025.119143.
[11] K. Hagihara, T. Nakano, Control of anisotropic crystallographic texture in powder bed fusion additive manufacturing of metals and ceramics—a review, JOM 74 (2021) 1760–1773, https://doi.org/10.1007/s11837-021-04966-7.
[12] T. Ishimoto, N. Morita, R. Ozasa, A. Matsugaki, O. Gokcekaya, S. Higashino, M. Tane, T. Mayama, K. Cho, H.Y. Yasuda, M. Okugawa, Y. Koizumi, M. Yoshiya, D. Egusa, T. Sasaki, E. Abe, H. Kimizuka, N. Ikeo, T. Nakano, Superimpositional design of crystallographic textures and macroscopic shapes via metal additive manufacturing—game-change in component design, Acta Mater. 286 (2025) 120709, https://doi.org/10.1016/j.actamat.2025.120709.
[13] P.V. Cobbinah, S. Matsunaga, Y. Toda, R. Ozasa, M. Okugawa, T. Ishimoto, Y. Liu, Y. Koizumi, P. Wang, T. Nakano, Y. Yamabe-Mitarai, Peculiar microstructural evolution and hardness variation depending on laser powder bed fusion-manufacturing condition in Ti–6Al–2Sn–4Zr–6Mo, Smart Mater. Manuf. 2 (2024) 100050, https://doi.org/10.1016/j.smmf.2024.100050.
[14] T. Mayama, T. Ishimoto, M. Tane, K. Cho, K. Manabe, D. Miyashita, S. Higashino, T. Kikukawa, H.Y. Yasuda, T. Nakano, Novel strengthening mechanism of laser powder bed fusion-manufactured Inconel 718: effects of customized hierarchical interfaces, Addit. Manuf. 93 (2024) 104412, https://doi.org/10.1016/j.addma.2024.104412.
[15] D.E. Jodi, T. Kitashima, Y. Koizumi, T. Nakano, M. Watanabe, Manufacturing single crystals of pure nickel via selective laser melting with a flat-top laser beam, Addit. Manuf. Lett. 3 (2022) 100066, https://doi.org/10.1016/j.addlet.2022.100066.
[16] O. Gokcekaya, T. Ishimoto, S. Hibino, J. Yasutomi, T. Narushima, T. Nakano, Unique crystallographic texture formation in Inconel 718 by laser powder bed fusion and its effect on mechanical anisotropy, Acta Mater. 212 (2021) 116876, https://doi.org/10.1016/j.actamat.2021.116876.
[17] Y. Li, Y.F. Yu, Z.B. Wang, X.Y. Liang, W.B. Ken, F. Lin, Additive Manufacturing of nickel-based superalloy single crystals with IN-738 alloy, Acta Metall. Sin.-Engl. 35 (2022) 369–374, https://doi.org/10.1007/s40195-021-01320-3.
[18] M.R. Gotterbarm, A.M. Rausch, C. Körner, Fabrication of single crystals through a μ-helix grain selection process during electron beam metal additive manufacturing, Metals 10 (2020) 313, https://doi.org/10.3390/met10030313.
[19] P. Fernandez-Zelaiae, M.M. Kirka, A.M. Rossy, Y. Lee, S.N. Dryepondt, Nickel-based superalloy single crystals fabricated via electron beam melting, Acta Mater. 216 (2021) 117133, https://doi.org/10.1016/j.actamat.2021.117133.
[20] P. Fernandez-Zelaia, M.M. Kirka, S.N. Dryepondt, M.N. Gussev, Crystallographic texture control in electron beam additive manufacturing via conductive manipulation, Mater. Des. 195 (2020) 109010, https://doi.org/10.1016/j.matdes.2020.109010.
[21] J. Yang, F. Li, A. Pan, H. Yang, C. Zhao, W. Huang, Z. Wang, X. Zeng, X. Zhang, Microstructure and grain growth direction of SRR99 single-crystal superalloy by selective laser melting, J. Alloys Compd. 808 (2019) 151740, https://doi.org/10.1016/j.jallcom.2019.151740.
[22] C. Körner, M. Ramsperger, C. Meid, D. Bürger, P. Wollgramm, M. Bartsch, G. Eggeler, Microstructure and mechanical properties of CMSX-4 single crystals prepared by additive manufacturing, Metall. Mater. Trans. A Phys. Metall. Mater. Sci. 49 (2018) 3781–3792, https://doi.org/10.1007/s11661-018-4762-5.
[23] S. Hibino, T. Todo, T. Ishimoto, O. Gokcekaya, Y. Koizumi, K. Igashira, T. Nakano, Control of crystallographic texture and mechanical properties of hastelloy-X via laser powder bed fusion, Crystals 11 (2021) 1–12, https://doi.org/10.3390/cryst11091064.
[24] Y. Liu, K. Nose, M. Okugawa, Y. Koizumi, T. Nakano, Fabrication and process monitoring of 316L stainless steel by laser powder bed fusion with μ-helix scanning strategy and narrow scanning line intervals, Mater. Trans. 64 (2023) 1135–1142, https://doi.org/10.2320/matertrans.mt-me2022006.
[25] M. Okugawa, K. Saito, H. Yoshima, K. Sawaizumi, S. Nomoto, M. Watanabe, T. Nakano, Y. Koizumi, Solute segregation in a rapidly solidified Hastelloy-X Ni-based superalloy during laser powder bed fusion investigated by phase-field and computational thermal-fluid dynamics simulations, Addit. Manuf. 84 (2024) 104079, https://doi.org/10.1016/j.addma.2024.104079.
[26] R.C. Reed, The Superalloys Fundamentals and Applications, Cambridge University, Cambridge, 2006.
[27] N. El-Bagoury, M. Waly, A. Nofal, Effect of various heat treatment conditions on microstructure of cast polycrystalline IN738LC alloy, Mater. Sci. Eng. A 487 (2008) 152–161, https://doi.org/10.1016/j.msea.2007.10.004.
[28] E. Balikci, R.E. Ferrell, A. Raman, Preferred orientations in the superalloy IN738LC after different aging heat treatments, Zeitschrift Fuer Met. Res. Adv. Tech. 90 (1999) 141–146, https://doi.org/10.1515/ijmr-1999-900208.
[29] MICRostructure Evolution Simulation Software, Phase-Field Software Package. Available online: https://www.micress.de (accessed on 15 April 2025).
[30] J. Eiken, B. Böttger, I. Steinbach, Multiphase-field approach for multicomponent alloys with extrapolation scheme for numerical application, Phys. Rev. E - Stat. Nonlinear, Soft Matter Phys. 73 (2006) 1–9, https://doi.org/10.1103/PhysRevE.73.066122.
[31] B. Böttger, M. Apel, M. Budnitzki, J. Eiken, G. Laschet, B. Zhou, Calphad coupled phase-field model with mechano-chemical contributions and its application to rafting of γ' in CMSX-4, Comput. Mater. Sci 184 (2020) 109909, https://doi.org/10.1016/j.commatsci.2020.109909.
[32] C. Kumara, A.R. Balachandramurthi, S. Goel, F. Hanning, J. Moverare, Toward a better understanding of phase transformations in additive manufacturing of alloy 718, Materialia 13 (2020) 100862, https://doi.org/10.1016/j.mtla.2020.100862.
[33] B. Böttger, M. Apel, Phase-field simulation of the formation of new grains by fragmentation during melting of an ABD900 superalloy, IOP Conf. Ser.: Mater. Sci. Eng. 1281 (2023) 012008, https://doi.org/10.1088/1757-899x/1281/1/012008.
[34] J.O. Andersson, T. Helander, L. Höglund, P. Shi, B. Sundman, Thermo-calc & DICTRA, computational tools for materials science, Calphad 26 (2002) 273–312, https://doi.org/10.1016/S0364-5916(02)00037-8.
[35] M. Rappaz, J.A. Dantzig, Solidification, first ed., EFPL Press, Lausanne, 2009.
[36] Thermo-Calc Software, Ni-Based Superalloys Database, Version 10. URL, http://www.thermocalc.com/products-services/databases/thermodynamic/.
[37] Thermo-Calc Software, Ni-alloys Mobility Database, Version 5. URL, https://www.thermocalc.com/products-services/databases/mobility/.
[38] M. Okugawa, H. Yoshima, Y. Liu, P. Wang, Y. Koizumi, T. Nakano, Single-track investigation of rapid solidification conditions of Hastelloy-X Ni-based superalloy in laser powder-bed fusion and applicability of columnar equiaxed transition criteria, Virtual Phys. Prototyp. 21 (2026) e2639906, https://doi.org/10.1080/17452759.2026.2639906.
[39] H. Amano, T. Ishimoto, K. Hagihara, R. Suganuma, K. Aiba, S.-H. Sun, P. Wang, T. Nakano, Impact of gas flow direction on the crystallographic texture evolution in laser beam powder bed fusion, Virtual Phys. Prototyp. 18 (2023), https://doi.org/10.1080/17452759.2023.2169172.
[40] S. Ghosh, J. Zollinger, M. Zaloznik, D. Banerjee, C.K. Newman, R. Arroyave, Modeling of hierarchical solidification microstructures in metal additive manufacturing: challenges and opportunities, Addit. Manuf. 78 (2023) 103845, https://doi.org/10.1016/j.addma.2023.103845.
[41] M. Okugawa, D. Izumikawa, Y. Koizumi, Simulations of non-equilibrium and equilibrium segregation in nickel-based superalloy using modified Scheil-Gulliver and phase-field methods, Mater. Trans. 61 (2020) 2072–2078, https://doi.org/10.2320/matertrans.mt-ma2020005.
[42] K. Karayagiz, L. Johnson, R. Seede, V. Attari, B. Zhang, X. Huang, S. Ghosh, T. Duong, I. Karaman, A. Elwany, R. Arróyave, Finite interface dissipation phase field modeling of Ni–Nb under additive manufacturing conditions, Acta Mater. 185 (2020) 320–339, https://doi.org/10.1016/j.actamat.2019.11.057.
[43] P. Kontis, E. Chauvet, Z. Peng, J. He, A.K. da Silva, D. Raabe, C. Tassin, J. J. Blandin, S. Abed, R. Dendievel, B. Gault, G. Martin, Atomic-scale grain boundary engineering to overcome hot-cracking in additively-manufactured superalloys, Acta Mater. 177 (2019) 209–221, https://doi.org/10.1016/j.actamat.2019.07.041.
[44] H. Chen, D. Egusa, Z. Li, T. Sasaki, R. Ozasa, T. Ishimoto, M. Okugawa, Y. Koizumi, T. Nakano, Phase-separation induced dislocation-network cellular structures in Ti-Zr-Nb-Mo-Ta high-entropy alloy processed by laser powder bed fusion, Addit. Manuf. 102 (2025) 104737, https://doi.org/10.1016/j.addma.2025.104737.